MINIREVIEW

🔄 Check for updates

Spin selectivity in chiral metal–halide semiconductors

Tanglue Feng, [ID] Zhiyu Wang, Zixuan Zhang, Jie Xue and Haipeng Lu [ID] *

Controlling the spin states of freedom represents a significant challenge for the next-generation opto-electronic and spintronic devices. Chiral metal–halide semiconductors (MHS) have recently emerged as an important class of materials for spin-dependent photonic and electronic applications. In this Minireview, we first discussed the chemical and structural diversity of chiral MHS, highlighting the chirality formation mechanism. We then provided our current understanding on the spin-sensitive photophysical and transport process with a focus on how chirality enables the spin selectivity in chiral MHS. We summarized recent progress on the experimental demonstration of spin control in various photonic and spintronic devices. Finally, we discussed ongoing challenges and opportunities associated with chiral MHS.

1. Introduction

In recent years, hybrid metal–halide semiconductors (MHS) have aroused extensive interests because of their rich chemical and structural diversity and superior optoelectronic properties including high extinction coefficient, tunable bandgap over a wide wavelength range, high carrier mobility, and long carrier lifetime *etc.*[1–3] MHS especially the most representative metal–halide per-

ovskites, in particular, have emerged as a revolutionary solution-processable semiconductor system because of their excellent optoelectronic properties as demonstrated in several seminal reports since 2009[4–6] on their photovoltaic performance. Recently, uniting chiral organics with inorganic MHS adds new degrees of complexity to the MHS, and presents new opportunities for chiroptic, chiroptoelectronic and spintronic applications where controlling spin state of freedom is a critical component.[7–12]

Chirality is an important structural property in many materials, such as amino acid, molecular drugs, macromolecules (DNA, peptide), and inorganic quantum dots, which are essential to their distinct functionality, including bio-

Department of Chemistry, The Hong Kong University of Science and Technology, Clear Water Bay, Kowloon, Hong Kong, China (SAR). E-mail: haipenglu@ust.hk

Tanglue Feng is currently a post-doctoral fellow at the Department of Chemistry of the Hong Kong University of Science and Technology (HKUST). He obtained his B.Sc. in chemistry from Lanzhou University in 2016, and received his Ph.D. in polymer chemistry and physics in 2021 under the supervision of Prof. Bai Yang at the State Key Laboratory of Supramolecular Structure and Materials of Jilin University. His current research interests are the structural chemistry, spin property and energy-related applications of chiral semiconductors.

Tanglue Feng

Haipeng Lu is an Assistant Professor at the Department of Chemistry of the Hong Kong University of Science and Technology (HKUST). His group works on developing inorganic chemistry approaches to address challenges related to renewable energy and sustainability. He received his B.Sc. in chemistry from Nanjing University in 2012, and completed his Ph.D. in 2017 in chemistry at the University of Southern California. He then moved to the National Renewable Energy Laboratory (NREL) as a postdoctoral fellow. He is the 2019 ACS Division of Physical Chemistry Young Investigator Awardee. His current research is focused on the molecular design of quantum-confined and chiral semiconductors for optoelectronic and spintronic applications.

Haipeng Lu

specific recognition, chiroptical activity, and optical/electronic applications.[8,9,11,13–17] The flexible crystal structure and tunable composition of MHS allow chiral organics to be intercalated into the metal–halide frameworks, or functionalized on their nanocrystal surface, thus expediently endowing MHS with chirality.[8,9,12] Compared with other chiral systems, such as organic small molecules, biomacromolecules and inorganic quantum dots, chiral MHS exhibit several advantages, including solution processability, suitable bandgaps, superior optical and electronic properties, and high spin selectivity.

Spin selectivity in chiral MHS is recently demonstrated in various optical and transport processes.[18–20] On one hand, chirality leads to chiroptical activity, namely circularly polarized absorption and/or emission, which carries ±1⟩ angular momentum. In semiconductors with strong spin–orbit coupling (SOC), angular momentum contains both spin and orbital angular momentum ($J = L + S$). As such, circular polarization carries spin information, namely, right- and left-polarized light, correspond to two spin states of photons in the quantum picture.[21] Chiral MHS thus enables spin control in optical absorption and/or emission. On the other hand, the strong SOC, long spin coherence lifetime and tunable Rashba splitting[7,12,22–27] when combined with chirality, results in highly spin-polarized charge transport through chiral MHS. As such, recent demonstration of spin-dependent charge transport in chiral MHS provides a new paradigm for spin manipulation.[20,28–30] Charge transport in chiral MHS is shown to be highly spin dependent, and such process can be modulated by the handedness of chiral MHS. The process is proposed to be mediated by chiral-induced spin selectivity (CISS) effect, which does not require cryogenic temperatures and high magnetic fields, thus affords new directions for spintronic applications. CISS effect[13,14,31–41] has been demonstrated in various chiral systems, such as organic small molecules,[34,38,42,43] biomacromolecules[37,44–46] and inorganic quantum dots.[47] Spin polarization mediated by CISS in chiral MHS appears to be much higher than those of chiral organic systems. Moreover, the structural asymmetry arising from the chiral space group (Sohncke space group) in chiral MHS also results in interesting non-linear optics (NLO)[48–50] and ferroelectricity.[51–54] Thus far, the family of chiral MHS have been rapidly expanded and have been investigated for circularly polarized luminescence, NLO, ferroelectricity, bulk photovoltaic effect, circularly polarized light (CPL) detection and opto-spintronic applications.[8–12]

In this Minireview, we summarized recent advances in the development of chiral MHS with a special focus on the spin selectivity in both optical and electrical transport processes. We discussed how the chirality endows spin control in this new family of materials, and the knobs that control the optical activity and spin selectivity, *i.e.*, the structure–property relationships. Recent demonstrations in spin-dependent optoelectronic and spintronic devices are then summarized. We concluded with an outlook on future directions in chiral MHS. We believed that our review would deepen the understanding of chiral MHS for spin-dependent optoelectronic applications, and provide research references for various chiral materials.

2. Chemical and structural design of chiral MHS

2.1. Composition and structure of chiral MHS

Based on their chemical composition and structure, MHS can be categorized into all-inorganic and hybrid organic–inorganic MHS. Three-dimensional (3D) MHS generally adopt the perovskite structure (ABX_3), with A cations occupying voids formed by BX_6 octahedra framework, where A sites are metal or organic cations including Cs^+, $CH_3NH_3^+$ (MA^+), $HC(NH_2)_2^+$ (FA^+), B sites contain divalent metal ions including (Pb^{2+}, Sn^{2+}, Ge^{2+} *etc.*), X represents halide anions (Cl^-, Br^- and I^-).[1,55,56] The choice of the A-site cation for a stable 3D perovskite structure is empirically determined by the Goldschmidt tolerance factor.[1,2,56] When the size of A cation (such as, long-chain alkyl amine or aromatic-containing structures) is larger than the constrained void, 3D metal–halide perovskite structure will condensate into lower dimensional structures, such as 2D, 1D and 0D structures, where the octahedron can be shared by corner-, edge-, face-mode, or a combination of different modes.[57,58] MHS, especially 3D metal–halide perovskite, can be prepared as bulk crystals, thin films, or nanocrystals.

The rich chemical, structural and morphological diversity can therefore grant chirality into the metal–halide lattices by introducing chiral organic cations/ligands. So far, chiral MHS have been reported in the form of chiral metal–halide crystals (where chiral organics are intercalated into metal–halide framework), chiral metal–halide thin films, and chiral metal–halide nanostructures. Chiral MHS are categorized into two types: intrinsic chiral crystal structures and chiral nanocrystals (NCs).[9,12] Correspondingly, there are mainly three strategies to construct chirality in MHS, including chiral organics-induced chirality in crystal structures, chiral surface ligands-induced chirality in NCs, and supramolecular assembly of NCs, as presented in the following section 2.2.

2.2. Chirality design of MHS

2.2.1. Chiral organics-induced chirality in crystal structures. The structural flexibility and diversity of MHS materials allows to incorporate numerous types of chiral organic cations (Fig. 1) to directly intercalate into the crystal lattices of MHS, which results in the deformation, distortion and/or helical arrangement of crystal structures. Thus, the molecular chirality of organic cations can be transferred to the crystal structure of metal–halide components, and the induced chirality is typically stronger than those in chiral QDs and metal NPs.[9] As such, chiral MHS materials can obtain appealing chiroptical properties including circular dichroism (CD) and circularly polarized light (CPL) emission, as well as nonlinear optical response, *etc.*[8–10] In recent years, a series of chiral MHS crystal structures (Table 1) including Pb–halide semiconductors and many Pb-free MHS based on various metals (such as, Sn,[28] Bi,[50,59–61] Ag–Bi,[59] Cu,[62–66] Mn,[53] Sb[50] and Cd[52,67,68]) were synthesized by introducing chiral organic cations.
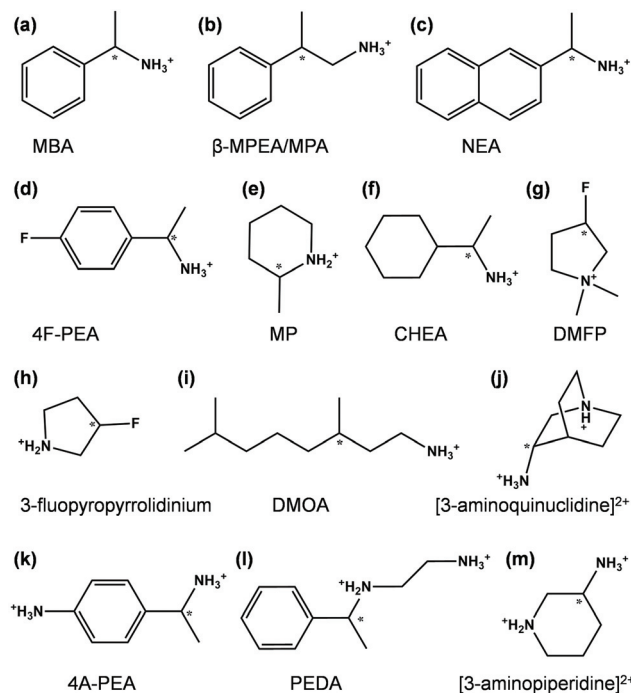
Fig. 1 The chemical structures of chiral organic cation ligands reported in literatures. "*" represents chiral center. MBA: methylbenzylammonium (also called as PEA or α-PEA); β-MPEA/MPA: β-methylphenethylammonium; NEA: 1-(1-naphthyl)ethylammonium; 4F-PEA: 4-fluorophenylethylammonium; MP: 2-methylpiperidinium; CHEA: 1-cyclohexylethylammonium; DMFP: N,N-dimethyl-3-fluoropyrrolidinium; DMOA: 3,7-dimethyloctylammonium; 4A-PEA: [(4-aminophenyl)ethylamine]$^{2+}$; PEDA: (1-phenylethyl)ethane-1,2-diaminium.

Most reported chiral MHS crystals display low-dimensional connectivity, including corner-shared 2D/quasi-2D, corner/edge/face-shared 1D, as well as edge-shared 0D octahedral structures as shown in Fig. 2. Chiral 3D MHS that are in a 3D perovskite structure, remain notably absent due to the small cuboctahedra cavity of 3D perovskites for suitable chiral organic cations. The most common chiral crystal structure is 2D perovskite structure with corner-shared metal–halide octahedron. Billing et al. first reported the synthesis and crystal structures of both 2D and 1D chiral hybrid organic–inorganic MHS by incorporating chiral aromatic MBA cation into lead-halide sublattice.[80] The crystal structure and intermolecular interactions, such as hydrogen bonding and π–π stacking, in 1D MBAPbX$_3$ (X = Cl, Br, I; face-shared Pb–halide octahedra), 1D (MBA)$_3$PbX$_5$ (X = Cl, Br; corner-shared octahedra), and 2D (MBA)$_2$PbI$_4$ consisting of corner-shared octahedral structures, were systematically investigated. Lu et al. prepared chiral 2D (R-/S-MBA)$_2$SnI$_4$ perovskites with corner-shared SnI$_6^{4-}$ octahedron (Fig. 2a) by incorporating chiral R-/S-MBA cations. The octahedron's bond length was found to be highly distorted, which stems from the hydrogen bonding between organic and inorganic sublattice.[28] The quasi-2D chiral MHS was also reported, such as (MPA)$_2$(MA)Pb$_2$I$_7$ perovskite[84] (Fig. 2b) which is composed of corner-shared [(MA$^+$)Pb$_2$I$_7$]$^{2-}$ bilayers separated by the double layers of interdigitated chiral MPA cations. In

addition, it was reported that the 1D MHS crystals exhibited rich structure diversity as shown in Fig. 2c–f. Billing and co-worker synthesized several 1D chiral MHS, including (MBA)$_3$PbX$_5$ (corner sharing, double chains), (MBA)$_8$Pb$_8$I$_{14}$ (corner-sharing, three chains), and MBAPbX$_3$ (face-sharing).[79,80] Peng et al. reported highly distorted 1D chiral C$_5$H$_{14}$N$_2$PbCl$_4$·H$_2$O MHS with edge-sharing [PbCl$_6$]$^{4-}$ octahedra by employing chiral 3-aminopiperidine cation.[83] Ishii and Miyasaka reported chiral 1D (NEA)PbI$_3$ MHS comprised of face-sharing (PbI$_6$)$^{4-}$ octahedral chains by employing chiral R/S-NEA$^+$ cation. They found that the large naphthalene skeleton in NEA$^+$ strongly influence the helicity of octahedral chains, which gives rise to intense CD signals in helical 1D (PbI$_6$)$^{4-}$ chains.[78] Chiral 0D MHS were reported with Sb- and Bi-halides in the form of A$_4$M$_2$X$_{10}$ as shown in Fig. 2g, which contains edge-sharing metal–halide octahedra dimer (M$_2$X$_{10}$)$^{4-}$.[50,60] 0D chiral (MBA)$_2$CuCl$_4$ crystals composed of single metal–halide tetrahedron unit[64] were also reported. The chiral organics can also be charge neutral, in the case of (MBA)$_4$Cu$_4$I$_4$ (Fig. 2h), where MBA cations coordinate to Cu center and form 0D chiral copper–iodide clusters.[65]

It is worth mentioning that chiral MHS structures can also be fabricated in chiral environments (such as solvents, templates) or special reaction conditions (such as temperature change), without chiral organic cations incorporated in the final product.[11,12] However, there are only few of these chiral crystal structures reported, and it is often composition specific.[87–89] For instance, Ohsumi et al. reported a phase transition process of CsCuCl$_3$ crystals from achiral P6$_3$/mmc space group to chiral enantiomorphic space groups (P6$_1$22, P6$_5$22; Fig. 3a) below T$_C$ = 423 K due to the Jahn–Teller effect on Cu^{2+} ions which leads to reduced lattice symmetry.[87]

2.2.2. Chiral MHS nanocrystals with chiral surface ligands. Chiral MHS can also be prepared in the form of NCs by surface modification with chiral organic ligands. Typically, chiral MHS NCs can be prepared either by direct synthesis with chiral organic ligands present in the reaction, or by a post-synthetic ligand-exchange reaction with chiral organic ligands. Kim et al. demonstrated that both strategies can be used to prepare chiral FAPbBr$_3$ NCs (Fig. 3b) using chiral R-2-octylamine or chiral MBA ligands. The resulted chiral perovskites showed high CPL emission with an average dissymmetry factor (g$_{lum}$) of 6.8 × 10^{-2}.[90] He et al. found that the chiroptical activity of as-obtained chiral CsPb(I/Br)$_3$ NCs prepared by post-ligand-exchange method depends on the amount of chiral ligands (chiral 1,2-diaminocyclohexane, DACH).[91] For a small amount of DACH, the chiroptical activity of CsPb(I/Br)$_3$ NCs mainly results from surface distortions, defects or/and electronic interaction. However, excessive amounts will result in the aggregation of chiral DACH on the surface of NCs, and thus the chiroptical activity of NCs is mainly contributed by DACH rather than surface distortions. Chen et al. employed chiral α-octylamine to modify CsPbBr$_3$ NCs, achieving two-photon absorption-based up-conversion CPL emission.[92] They attributed their chiroptical activity of CsPbBr$_3$ NCs to the surface lattice distortion induced by chiral capping ligands.

Table 1 The compositions, structures and properties of chiral MHS crystals prepared from chiral organics

Metal cation	chiral organic cation	Dimensionality	Composition	Property	$g_{CD}/g_{lum}/g_{res}/g_{Iph}$	Ref.
Pb^{2+}	MBA^+ NEA^+	2D-corner	$(MBA)_2PbI_{4(1-x)}Br_{4x}$ $(NEA)_2PbI_{4(1-y)}Br_{4y}$	CD	—	69
	MBA^+	2D-corner	$(MBA)_2PbI_4$	CD, spin-polarized charge transport	—	20
	MBA^+	2D-corner	$(MBA)_2PbI_4$	CD, CPL emission, CPL detection	$g_{lum} = 0.352$	70
	$(X\text{-}MBA)^+$ $(X = F, Cl. Br, I)$	2D-corner	$(X\text{-}MBA)_2PbI_4$ $(X = F, Cl. Br, I)$	CD, CPL emission	—	71
	PEA^+	2D-corner	$(PEA)_2PbI_4$	CD, CPL emission, CPL detection	$g_{lum} = 0.274$, $g_{res} = 0.23$	72
	PEA^+	2D-corner	$(PEA)_2PbI_4$	Linear/circular polarization light detection	$g_{res} = 0.15$	73
	$4\text{-}Br\text{–}PEA^+$	2D-corner	$(4\text{-}Br\text{–}PEA)_2PbI_4$	CD, CPL detection	$g_{CD} = 0.003$, $g_{Iph} = 0.13$	74
	$\beta\text{-}MPEA^+$	2D-corner	$(\beta\text{-}MPEA)_2PbBr_4$	CD, white CPL emission	—	75
	$PEDA^{2+}$	2D-corner	$(PEDA)PbI_4$	Vibrational CD, ferroelectricity, ferroelasticity	—	51
	$4A\text{-}PEA^{2+}$	2D-corner	$(4A\text{-}PEA)PbI_4$	CD, CPL emission, heat/pressure-dependent PL	$g_{CD} = 0.0001$, $g_{lum} = 0.075$	76
	MBA^+	2D-corner 1D-face	$(MBA)_2PbI_4$ $MBAPbX_3 (X = Br, I)$	CD, CPL emission, NLO	—	77
	NEA^+	2D-corner 1D-face	$(NEA)_2PbI_4$ $(NEA)PbI_3$	CD, CPL detection	$g_{CD} = 0.04$, $g_{res} = 1.85$	78
	MBA^+	1D-corner 1D-face	$(MBA)_8Pb_8I_{14}$ $MBAPbBr_3$	—	—	79
	MBA^+	1D-corner	$(MBA)_3PbX_5 (X = Cl, Br)$	—	—	80
	PEA^+	1D-face	$PEAPbI_3$	CD, CPL detection	$g_{CD} = 0.02$, $g_{res} = 0.1$	81
	MP^+	1D-face	$(MP)PbX_3 (X = Br, I)$	NLO, dielectric switching	—	82
	$CHEA^+$	1D-face	$(CHEA)PbI_3$	Ferroelectric and pyroelectric properties	—	54
	$[3\text{-}Aminopiperidine]^{2+}$	1D-edge (single chain)	$(3\text{-}Aminopiperidine)_2PbI_4$	NLO	$g_{SHG\text{–}CD} = 0.21$	48
	$\beta\text{-}MPEA^+$	1D-edge (single chain)	$(\beta\text{-}MPEA)_{1.5}PbBr_{3.5}(DMSO)_{0.5}$	NLO	—	49
	$[3\text{-}Aminopiperidine]^{2+}$	1D-edge (double chain)	$(C_5H_{14}N_2)PbCl_4 \cdot H_2O$	CD, CPL emission, NLO	—	83
	$\beta\text{-}MPEA^+, MA^+$	Quasi 2D-corner	$(\beta\text{-}MPEA)_2MAPb_2I_7$	Spin photovoltaic effect	—	84
	$\beta\text{-}MPEA^+, MA^+$	Quasi 2D-corner	$(\beta\text{-}MPEA)_2MAPb_2I_7$	CD, CPL detection	$g_{Iph} = 0.2$	85
	MBA^+, MA^+	Quasi 2D-corner	$n = 2$	CD, CPL emission	$g_{CD} = \sim0.001$, $g_{lum} = 0.06$	19
Pb^{2+}, Cs^+	NEA^+	Quasi 2D-corner	$n = 2$	CD, CPL emission	$g_{lum} = 0.002$	86
Pb^{2+}, Sn^{2+}	MBA^+	2D-corner	$(MBA)_2Pb_{1-x}Sn_xI_4$ $(MBA)_2SnI_4$	CD, spin-polarized charge transport	—	28
Pb^{2+}/Cu^{2+}	$\beta\text{-}MPEA^+$ $DMOA^+$	2D-corner	$(\beta\text{-}MPEA)_2CuX_4$ $(DMOA)_2CuX_4$ $(DMOA)_2PbX_4$ $(X = Cl, Br)$	Dielectric phase transition	—	66
Cu^{2+}	MPA^+	2D-corner	$(MPA)_2CuCl_4$	Ferromagnetism	—	62
	$[3\text{-}Aminoquinuclidine]^{2+}$	1D-Corner (hexahedron)	$(C_7H_{16}N_2)CuX_4 (X = Cl, Br)$	NLO, temperature phase transitions	—	63
	MBA^+	0D cluster (tetrahedron)	$(MBA)_2CuCl_4$	CD, CPL emission	$g_{CD} = \sim0.1$, $g_{res} = 0.21$	64
	MBA^+	0D cluster (tetrahedron)	$(MBA)_4Cu_4I_4$	CD, CPL emission	$g_{lum} = 0.01$	65
Bi^{3+}	MBA^+	0D-edge	$(MBA)_4Bi_2Br_{10}$	CD, NLO	—	60
	MBA^+	1D-edge (single chain)	$(MBA)BiI_4$	CD, NLO	—	61
Bi^{3+}/Sb^{3+}	$4F\text{-}PEA^+$	0D-edge	$(4F\text{-}PEA)_4Bi_2X_{10}$ $(4F\text{-}PEA)_4Sb_2X_{10}$ $(X = Cl, Br, I)$	NLO	—	50
Bi^{3+}, Ag^+	$\beta\text{-}MPEA^+$	2D-corner	$(\beta\text{-}MPA)_4AgBiI_8$	CD, CPL detection	$g_{CD} = 0.0014$, $g_{Iph} = 0.22$	59
Cd^{2+}	$MPPA^+$	0D-edge 1D-corner	$[MPPA]_2CdCl_4$ $[MPPA]_2CdCl_4$	CD, NLO, ferroelectricity	—	67
	3-Fluoropyrrolidinium	1D-face	$3\text{-}(Fluoropyrrolidine)CdCl_3$	Vibrational CD, ferroelectricity	—	52
	$DMFP^+$	1D-face	$(DMFP)CdCl_3$	Vibrational CD, dielectric switching	—	68

Table 1 (*Contd.*)

Metal cation	chiral organic cation	Dimensionality	Composition	Property	$g_{CD}/g_{lum}/g_{res}/g_{Iph}$	Ref.
Mn^{2+}	3-Fluoropyrrolidinium	1D-face	3-(Fluoropyrrolidine)MnBr$_3$	Vibrational CD, CPL emission, ferroelectricity	g_{lum} = 0.006	53

MPPA$^+$: [1-methyl-3-phenylpropylamine]$^+$; g_{CD}: anisotropy factor of CD, g_{CD} = CD (mdeg)/(32 980 × A_{linear}); g_{lum}: dissymmetry factor of CPL emission (I), g_{lum} = 2 × (I_L − I_R)/(I_L + I_R); g_{res}: anisotropy factor of photoresponsivity (R), g_{res} = 2 × (R_L − R_R)/(R_L + R_R), in which $R = I_{ph}/P$; g_{SHG-CD}: anisotropy factor of second harmonic generation signal (I_{SHG}), g_{SHG-CD} = 2 × (I_{L-SHG} − I_{R-SHG})/(I_{L-SHG} + I_{R-SHG}); g_{Iph}: dissymmetry factor of photocurrent (I), g_{Iph} = 2 × (I_L − I_R)/(I_L + I_R). Subscripted L and R represent the left and right-handed circularly polarized lights, respectively. The biggest values of g_{lum}, g_{res}, g_{Iph} and g_{SHG-CD} are 2.0.
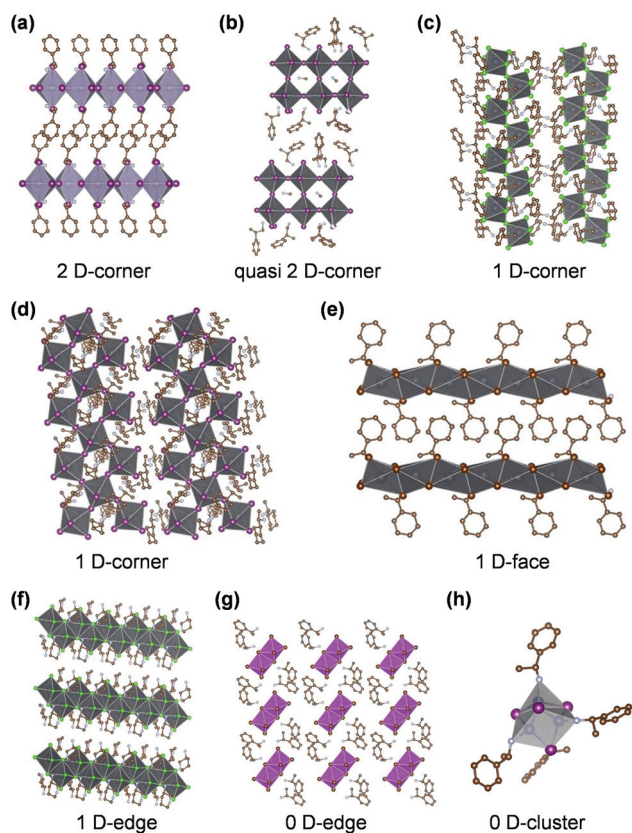

Fig. 2 Schematic illustration of crystal structures of chiral MHS prepared by chiral organics-induced method.

2.2.3. Supramolecular assembly of nanocrystals. MHS can also obtain chiroptical activities by supramolecular assembly with chiral mediators, such as chiral gelators,[93] liquid crystals,[94,95] or helical polymer.[96] For instance, Shi *et al.* mixed achiral all-inorganic CsPbX$_3$ NCs (X = Cl, Br, I) with the chiral organic gelator of *N,N′*-bis(octadecyl)-ʟ-glutamic diamide (LGAm) or its enantiomer (DGAm) in nonpolar solvents to fabricate cogels (Fig. 3c), endowing NCs with the CPL-emission property.[93] The chirality transfer was ascribed to well-ordered organization of CsPbX$_3$ NCs along the chiral assemblies. Yang *et al.* combined CsPbBr$_3$ NCs with chiral liquid crystal and up-conversion nanoparticles, obtaining assembled chiral CsPbBr$_3$-based hybrids with up-conversion CPL emission.[95] It

should be noted that the MHS-NCs can also be endowed with chiroptical activity through helical arrangement. Liu *et al.* employed dried inorganic silica nanohelices film as templates to arrange helically CsPbBr$_3$ NCs (Fig. 3d), inducing chiroptical properties with a large CD and CPL-emission signals (a dissymmetric factor of up to 6 × 10^{-3}).[97]

3. Spin selectivity in optical process of chiral MHS

In semiconductor spintronics, CPL is often used as a means for spin injection or spin readout. When excited by circularly polarized photon, electron–hole pairs or an exciton are created in semiconductors, which process follows optical selection rules while preserving angular momenta. For instance, in traditional GaAs semiconductor, the angular momentum is conserved in the optical transition in the way that a circularly polarized photon with angular momentum −1 (+1) for σ^- (σ^+) polarization, creates an electron with spin $+\frac{1}{2}$ ($-\frac{1}{2}$) and a heavy hole (HH) with total angular momentum of +3/2 (−3/2). Similarly, σ^- (σ^+) polarization can also generate spin $-\frac{1}{2}$ ($+\frac{1}{2}$) electron and a light hole (LH) with angular momentum of $+\frac{1}{2}$ ($-\frac{1}{2}$) (Fig. 4a). As such, with circularly polarized photon excitation, spin-polarized carriers can be selectively generated, and semiconductors provide a platform for photon polarization and spin orientation interconversion.

In Pb–halide based MHS, the electronic structure forms a simpler two-level system. The large SOC yields a doubly degenerate $J_e = \frac{1}{2}$ level for electrons and $J_h = \frac{1}{2}$ for holes. In this scenario, CPL excites optical transitions with $\Delta m_J = 1$ (σ^-) or −1 (σ^+), namely $|\sigma^-\rangle \to |-\frac{1}{2}\rangle_e \otimes |+\frac{1}{2}\rangle_h$ and $|\sigma^+\rangle \to |+\frac{1}{2}\rangle_e \otimes |-\frac{1}{2}\rangle_h$ (Fig. 4b). It can be seen that in MHS, CPL leads to 100% spin polarization. However, in achiral MHS, the optical transition strengths for σ^- and σ^+ transitions are exactly the same, and there is no spin selectivity in achiral MHS. In chiral MHS, however, the induced chirality results in optical activity in inorganic frameworks, namely the optical excitonic transition strengths for σ^- and σ^+ are now different (Fig. 4c) and circularly polarized absorption and/or emission can be observed and measured as CD and/or CPL emission. These processes thus become spin-dependent in chiral MHS.
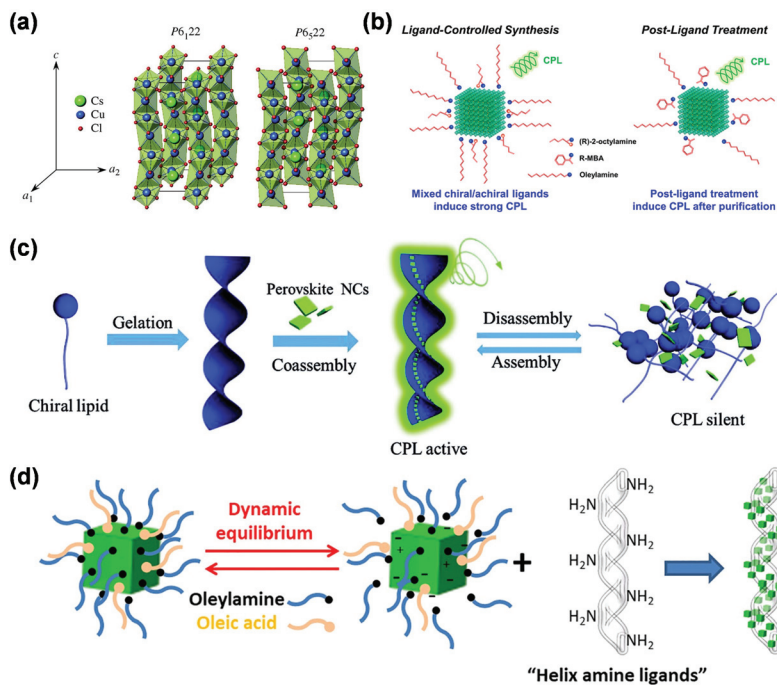
Fig. 3 (a) Schematic illustration of enantiomorphic crystal structures of CsCuCl$_3$. This figure has been adapted/reproduced from ref. 87 with permission from Wiley-VCH, Copyright 2013. (b) The post-treatment induced chirality in perovskite NCs by ligand exchange with chiral organic molecules. This figure has been adapted/reproduced from ref. 90 with permission from American Chemical Society, Copyright 2020. (c) Schematic illustration of assembly-induced chirality in perovskite NCs by chiral gels. This figure has been adapted/reproduced from ref. 93 with permission from Wiley-VCH, Copyright 2018. (d) Schematic illustration of the synthesis of chiral helical CsPbBr$_3$ NCs arranged on inorganic silica nanohelices. This figure has been adapted/reproduced from ref. 97 with permission from American Chemical Society, Copyright 2020.
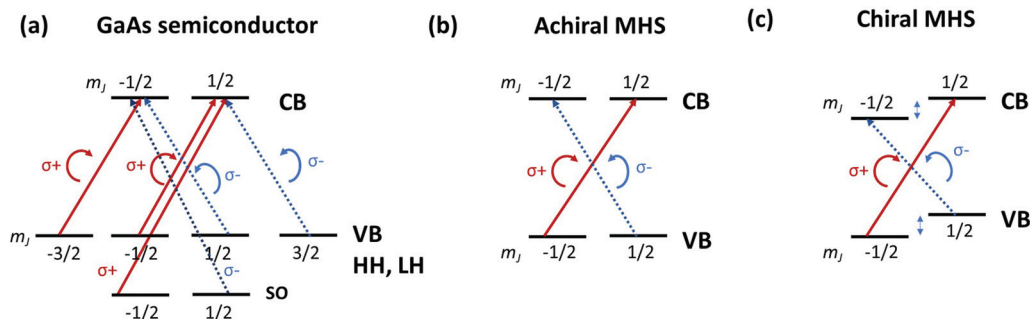

Fig. 4 Spin-dependent optical transitions in GaAs, achiral MHS and chiral MHS.

3.1. Spin-polarized absorption (circular dichroism, CD)

Left-handed circularly polarized (LCP) and right-handed circularly polarized (RCP) lights represent two different spin states of angular momentum. Typically, incident CPL can induce an electric transition dipole moment (ETDM, μ) because of the displacement of electrical charge along with rotation direction. When the LCP/RCP lights interact with the chiral photonic materials, the electrons are excited by specific excitonic transitions, thus preferentially absorbing LCP or RCP light based on the redistribution of helical electron clouds, which are accompanied with a circulation of charge and therefore the formation of a magnetic dipole transition moment (MTDM,

m).[9] This differential absorption for LCP and RCP lights is called as CD or Cotton effect. It has been demonstrated that chiral MHS can displays spin-polarized absorption which can be measured by electronic CD (ECD) spectroscopy.

The CD character of metal–halide perovskites was firstly reported in 2017. Ahn et al. investigated the chiroptical properties of 2D (R-/S-MBA)$_2$PbI$_4$ (Fig. 5a) and (rac-MBA)$_2$PbI$_4$ (rac: racemic mixture) thin films with different thicknesses and morphologies.[18] As shown in Fig. 5b, distinct CD signals were observed in (R-/S-MBA)$_2$PbI$_4$, with the same peak locations but opposite signals, while (rac-MBA)$_2$PbI$_4$ perovskite exhibited no CD signals. The CD signals of (R-/S-MBA)$_2$PbI$_4$ were also obviously different from those of R-/S-MBA (Fig. 5c), suggesting
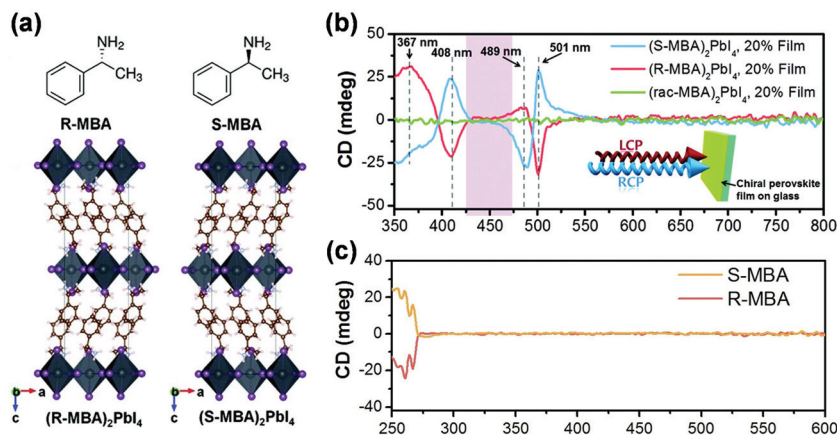
Fig. 5 (a) Schematic illustration of the crystal structures of $(R\text{-}/S\text{-MBA})_2PbI_4$ perovskites. (b) The CD spectra of $(R\text{-}/S\text{-MBA})_2PbI_4$ and $(rac\text{-MBA})_2PbI_4$ films. (c) The CD spectra of $R\text{-}/S\text{-MBA}$. This figure has been adapted/reproduced from ref. 18 with permission from Royal Society of Chemistry, Copyright 2017.

that the chiroptical properties were transferred into perovskite from chiral organic cations. In addition, CD signal of chiral $(MBA)_2PbI_4$ perovskite films can be altered by changing the crystalline orientation and thickness of perovskite film. The anisotropy factor of CD that is calculated by the equation: g_{CD} = CD (mdeg)/$(32\,980 \times A_{linear})$, can be employed to evaluate the CD strength. Currently, researchers have achieved decent g_{CD} values in some chiral MHS, such as, 0.02 for MBAPbI$_3$,[81] 0.04 for NEAPbI$_3$,[78] and 0.1 for $(MBA)_2CuCl_4$.[64]

The CD signals of chiral MHS can also be manipulated by composition and electronic structure engineering. It was reported that the intensity of CD signal can be tuned by changing their crystalline structure[77] and amounts of chiral organic molecule in MHS thin films,[91] and engineering organic cation (such as, 4-F/Cl/Br/I-MBA).[71] Dang *et al.* found that the CD signals of S-/R-MBAPbBr$_3$ single crystals are stronger and exhibited obvious red-shifting compared to those of their powders.[77] Furthermore, the composition engineering was demonstrated to be an effective strategy to endow MHS with tunable CD over a wide wavelength range. Ahn *et al.* found that the changes of the mixing ratio of bromide to iodide anions in $(S\text{-}/R\text{-MBA})_2PbI_{4(1-x)}Br_{4x}$ and $(S\text{-}/R\text{-NEA})_2PbI_{4(1-x)}Br_{4x}$ thin films can modulate the excitonic band structures of chiral perovskites, with the CD signals varying from 495 to 375 nm.[69] Lu *et al.* achieved the modulation of bandgap and chiroptical activity by alloying Sn with Pb in the series of 2D $(MBA)_2Pb_{1-x}Sn_xI_4$ perovskites.[28] Recently, researchers reported many chiral low-dimensional MHS materials from various metal cations and organic cations as shown in Table 1, which exhibited distinct CD activity. Additionally, perovskite NCs[90–92] modified by chiral ligands were also demonstrated to exhibit CD character. However, the design principles that relate the structure, composition, and dimensionality to the optical activity of chiral MHS remains unsolved.

3.2. Spin-polarized circularly polarized light emission

The excited state of chiral MHS upon circularly polarized light photoexcitation will undergo radiative recombination to ground state while preserving angular momenta (if the radiative recombination occurs prior to spin flip), generating CPL emission. The CPL emission and CD properties are two opposite optical phenomena, reflecting the electronic properties of the excited state and ground states, respectively. The CPL emission can be quantified by the dissymmetry (g_{lum}) factor as defined in equation: $g_{lum} = 2 \times (I_{left} - I_{right})/(I_{left} + I_{right})$, in which I_{left} and I_{right} represent the intensity of left- and right-handed CPL emission, respectively.

Chiral low-dimensional MHS crystals or thin films have been demonstrated to exhibit distinct CPL emission due to the induced chirality from embedded chiral organic cations. Long *et al.* first observed CD and CPL emission in chiral quasi-2D perovskites. A 3% CPL emission was observed without an applied external magnetic field.[19] Ma *et al.* reported CPL emission property in chiral 2D $(R\text{-}/S\text{-MBA})_2PbI_4$ perovskites as shown in Fig. 6.[70] The $(R\text{-MBA})_2PbI_4$ and $(S\text{-MBA})_2PbI_4$ perovskites exhibited an average g_{lum} of 0.192 and 0.202 at 77 K, respectively, and the g_{lum} showed a sharp decrease with the increase of temperature owing to spin relaxation. CPL emission properties were also revealed in other types of chiral MHS crystal structures, such as 2D $(4A\text{-PEA})PbI_4$,[76] quasi-2D perovskite thin films prepared from $R\text{-}/S\text{-NEABr}$ cations and CsBr and PbBr$_2$,[86] 1D MBAPbBr$_3$,[77] 1D [3-(fluoropyrrolidinium)]MnBr$_3$,[53] and 0D $(MBA)_4Cu_4I_4$.[65] Moreover, white CPL emission was also reported in some chiral MHS systems, such as chiral 1D $C_4N_2H_{14}PbI_4$,[72] 1D $C_5H_{14}N_2PbCl_4\cdot H_2O$,[83] and 2D $(\beta\text{-MPEA})_2PbBr_4$,[75] whose broad emissions were attributed to the coexistence of free excitons and self-trapped excitons. In addition, the up-conversion CPL emission were obtained in chiral CsPbBr$_3$ NCs.[92,95] For example. Yang *et al.* reported the intriguing phenomenon in the assembled chiral CsPbBr$_3$ NC hybrids based on a radiative energy transfer mechanism by incorporating up-conversion nanoparticles and achiral nematic liquid crystal with a dopant of chiral molecule.[95] The dissymmetry factor (g_{lum}) of their up-conversion CPL emission can be amplified to 1.1.
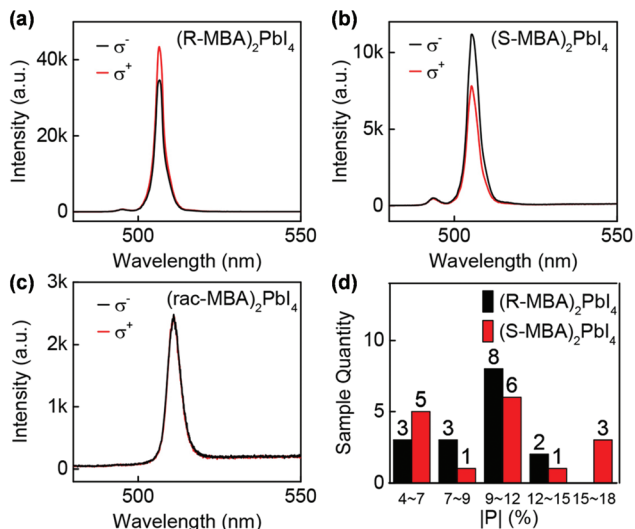
Fig. 6 (a–c) The circularly polarized PL spectra of $(R\text{-MBA})_2\text{PbI}_4$, $(S\text{-MBA})_2\text{PbI}_4$ and $(rac\text{-MBA})_2\text{PbI}_4$, respectively under excitation of 473 nm laser at 77 K. (d) Statistical histogram of the degree of CPL emission (P) for $(R\text{-}/S\text{-MBA})_2\text{PbI}_4$. This figure has been adapted/reproduced from ref. 70 with permission from American Chemical Society, Copyright 2019.

4. Spin selectivity in electron transport of chiral MHS

Apart from the spin-selective optical process, recent experimental results also demonstrated that charge transport through chiral MHS is also spin-dependent, which process is proposed to be mediated by the so-called chiral-induced spin selectivity (CISS) mechanism.

4.1. The concept and generation of CISS effect

For chiral molecules, the electron spin is intensively coupled with the molecular frame, and the transfer/transport of spin-polarized electron through chiral molecules depends on the enantiomeric handedness of molecule and the spin direction of electron, which is described as the CISS effects.[31,33,34,36,39,40,98] CISS effect is generated by the coupling between the linear momentum of an electron and its spin in a chiral material.[31,39] A simple physical model can be described as follows. When electrons move through a chiral medium, the electron current generates an effective magnetic field, $\vec{B}$, that acts on the electrons' intrinsic magnetic moment:

$$\vec{B} = \frac{\vec{v}}{c^2} \times \vec{E}_{\text{chiral}}$$

in which $\vec{v}$ is the velocity of the moving electron, c is the speed of light, and $\vec{E}_{\text{chiral}}$ is the electric field that acts on the electron while it moves through the chiral molecule (Fig. 7a).[39] As such, electrons with one specific spin direction are more easily to traverse/transport than ones with the opposite spin direction in chiral materials as shown in Fig. 7b, and the preferred spin polarization will change with the handedness of chiral materials and the direction of the electrons' linear momentum.[28,31,34,99,100]

CISS effect was first demonstrated by electron transmission experiments in self-assembled monolayers (SAM) of chiral molecules by Naaman's group.[43] They found that the transmission of photoelectrons through chiral Langmuir–Blodgett (LB) thin films composed of either L- or D-stearoyl lysine was spin-dependent, with the chiral molecules acting as a spin filter. Subsequently, spin-dependent electron transmission or electron transport properties were observed in many other chiral systems, such as, ds-DNA,[37] bacteriorhodopsin embedded in purple membrane,[46] oligopeptides,[101] cysteine-capped QDs,[47] bacterial cell surface,[102] conductive polymer,[103] metal–organic phenylalanine,[104] *etc.* Naaman and co-workers, in particular, carried out many pioneering works relevant to CISS effects.[37,38,43,99,101,104–107] In addition, CISS effects on the charge transfer processes were also demonstrated in some
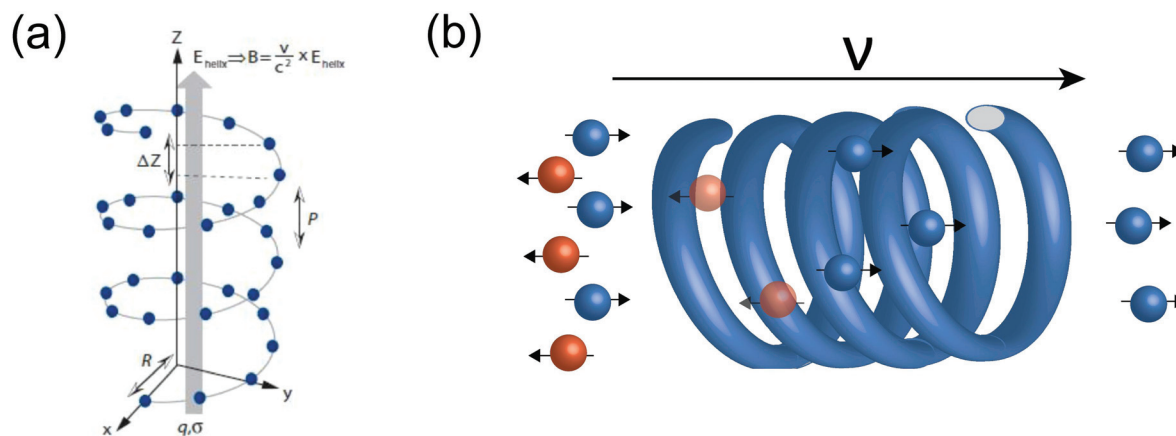

Fig. 7 Schematic illustration of the CISS process. The figure (a) has been adapted/reproduced from ref. 39 with permission from American Chemical Society, Copyright 2012.

photoinduced/electrochemical systems[41,45,106,107] as well as chemical reaction.[108]

4.2. CISS effect in chiral MHS

The generally available organic molecules are with small spin–orbit coupling (SOC) interaction, and the electron spin is weakly coupled with the molecule frame even when an external magnetic field is applied to orient them.[31,34] Thus, the spin control on chiral organic molecules is relatively difficult to generate considerable spin selectivity.[39] However, in chiral MHS, the induced chirality can be coupled with strong SOC and large Rashba splitting, obtaining unique chirality-dependent optoelectronic properties by CISS effects.

4.2.1. Spin-dependent charge transport. In 2019, Lu et al. demonstrated CISS effect on charge transport within 2D-layerd chiral Pb–I perovskite systems $(R\text{-}/S\text{-}MBA)_2PbI_4$. They measured a spin-dependent charge transport in chiral $(R\text{-}/S\text{-}MBA)_2PbI_4$ thin films by conductive-probe atomic force microscopy (mCP-AFM) with an ferromagnetic (FM) tip (Co–Cr coated) as shown in Fig. 8a. The FM tip was aforehand magnetized with permanent magnet, which can lead to different magnetization directions (up or down relative to the substrate of FTO).[20] When an electric bias potential was applied, the electrical current reflected electron transport from the substrate to FM tip through chiral perovskite films. According to the current–voltage (I–V) curves (Fig. 8b–d) for different chiral 2D perovskite films under different FM tip magnetization directions, it was suggested that the magnetization of probe tip and the handedness of chiral perovskites can influence the charge transport through chiral perovskite films. They defined a spin polarization of $P = (I^+ - I^-)/(I^+ + I^-) \times 100\%$, in which I^+ and I^-

represent the currents at specific potential under FM tip with up- and down-magnetization directions, respectively. Their measured spin-polarization degree (P) is up to 86%, which is higher than that of reported chiral self-assembled monolayer (SAM) systems (30–50%). The spin-dependent charge transport was also further validated in perovskite-based spin-valve devices. Furthermore, Lu et al. also demonstrated CISS effect in chiral 2D layered tin iodide perovskites, $(R\text{-}/S\text{-}MBA)_2SnI_4$.[28] The oriented tin-iodide perovskite films exhibited a highly spin-dependent vertical charge transport, achieving a spin-polarization degree of 94% for current enhancement in $(R\text{-}MBA)_2SnI_4$, which was ascribed to the effect of the spin-filtering from the oriented chiral organic molecules. Subsequently, Yang and co-workers also demonstrated similar spin-dependent charge transport in 1D chiral $(R\text{-}/S\text{-}MBA)PbBr_3$ with a spin-polarization efficiency of 90%.[29]

4.2.2. Spin-dependent magneto-optic Kerr effect. In addition to the electron transport measurements, CISS in MHS can also be measure by Sagnac magneto-optic Kerr effect (MOKE) experiment (Fig. 9a), in which a Sagnac interferometer with a laser beam is employed to probe the magnetization.[109] Under illumination of laser for ITO/chiral–MHS/ferromagnetic NiFe and an applied external magnetic field, a changed Kerr signals namely spin-polarized photocurrent can be observed. Specifically, the Kerr signals can be switched by changing the enantiomeric forms of chiral MHS or the magnetic field directions, as shown in Fig. 9b–d. The photoinduced change in the Kerr angle exhibit a linear dependence on the magnetic field with the slope determined by the chirality of MHS. These results suggested the existence of CISS effect on the interfacial magnetization of MHS–NiFe heterostructures, which provided a platform to precisely measure the strength of CISS.
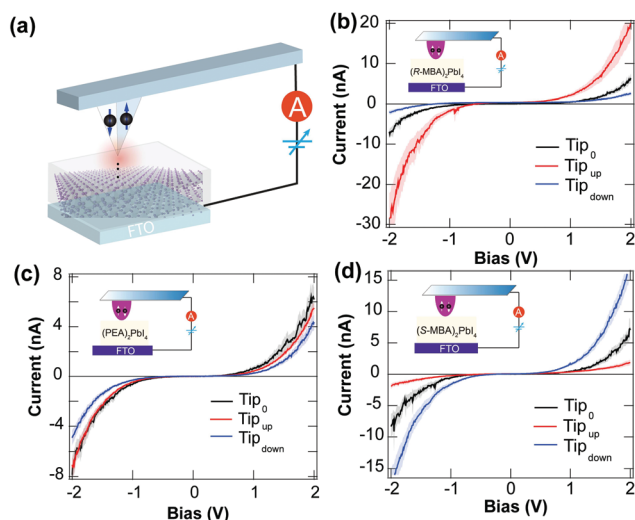

Fig. 8 (a) Schematic illustration of mCP–AFM measurement setup, and (b–d) chirality-dependent out-of-plane charge transport based on 2D hybrid perovskite thin films of $(R\text{-}MBA)_2PbI_4$, $(S\text{-}MBA)_2PbI_4$, and achiral $(PEA)_2PbI_4$, respectively. This figure has been adapted/reproduced from ref. 20 with permission from Science, Copyright 2019.
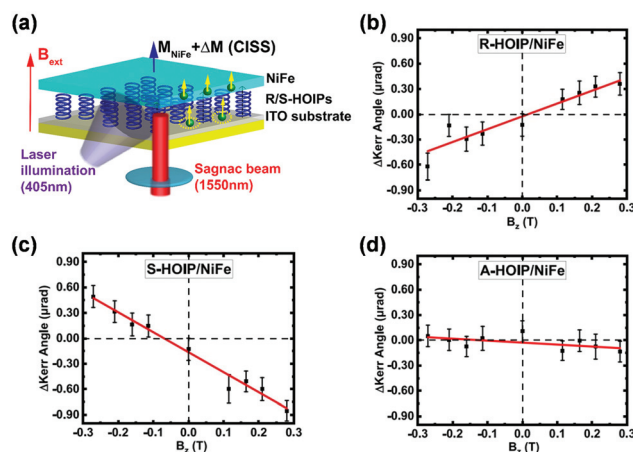

Fig. 9 (a) Schematic illustration of Sagnac MOKE experiment for the light-driven CISS effects-induced interfacial magnetization. (b−d) The measured Kerr signals upon laser illumination for (b) $R\text{-}MBA_2PbI_4$/NiFe, (c) $S\text{-}MBA_2PbI_4$/NiFe and (d) achiral MBA_2PbI_4/NiFe under positive/negative external magnetic field. This figure has been adapted/reproduced from ref. 109 with permission from American Chemical Society, Copyright 2020.

5. Spin-related optoelectronic devices based on chiral MHS

5.1. Spin-dependent photodetectors

The chiroptical properties of chiral MHS enable them as promising candidates for spin-dependent photonics devices, such as CPL detectors. Traditional photodetectors were often coupled with optical polarizers, limiting their sensitivity and resolution of CPL detection. Direct CPL detection can be achieved in chiral systems that exhibit large intrinsic CD. In CPL detectors, direct CPL detection requires to effectively convert the CD characteristic into adequately large electrical signals and amplify the discrimination (anisotropy factor) between left- and right-handed CPLs. Therefore, high-performance CPL photodetectors based on chiral materials require high photocurrent (I_{ph}) amplitude, large photoresponsivity (R) and anisotropy factor of responsivity (g_{res}), as well as low operating voltages. The R and g_{res} can be calculated by $R = I_{ph}/P$ and $g_{res} = 2 \times (R_L - R_R)/(R_L + R_R)$, in which P is the incident light power, and R_R and R_L represent the responsivities under right and left-handed CPLs.

Chiral low-dimensional MHS with strong chiroptical activity were recently demonstrated to construct CPL photodetectors, including 2D R-α-(PEA)$_2$PbI$_4$,[72] 2D (R-Br–PEA)$_2$PbI$_4$,[74] 1D (R-/S-α-PEA)PbI$_3$,[81] and 1D (S-NEA)PbI$_3$.[78] Chen et al. synthesized 1D chiral (R-/S-α-PEA)PbI$_3$ single crystals with CD properties.

Their chiral MHS was used to construct CPL photodetectors (Fig. 10a–c) which show relatively inferior responsivity of 120 mA W^{-1}, and a maximum g_{res} of 0.1.[81] Ishli developed helical 1D (S-NEA)PbI$_3$-based photodiodes for direct CPL detection (Fig. 10d and e), with a high responsivity of 0.28 and g_{res} of 1.85 achieved.[78] Peng et al. realized Vis-NIR dual-modal CPL detection with chiral 2D (R-BPEA)$_2$PbI$_4$ perovskite single crystals based on a two-photon absorption process.[74] These low-dimensional chiral MHS-based photodetectors tend to require high working voltages with relatively low output current generated because of poor or negligible conductivity. Design of heterostructures composing of high-mobility semiconductors to promote the charge transport properties was an effective strategy to improve the performance of CPL detectors. For example, Ma et al. constructed CPL photodetector on the basis of the hBN/(R-/S-MBA)$_2$Pb$_2$I$_4$/MoS$_2$ heterostructure, and the photoresponsivity and specific detectivity can reach to 450 mA W^{-1} and 2.2×10^{11} Jones, respectively.[70] Other metal-based chiral MHS such as 0D (MBA)$_2$CuCl$_4$ were also reported to fabricate CPL photodetectors in a heterostructure consisted of (MBA)$_2$CuCl$_4$ and SWCNT.[64] Excited electrons in chiral 0D (MBA)$_2$CuCl$_4$ by left/right-handed CPL can be rapidly transferred to SWCNT layer as show in Fig. 10f, thus providing superior polarization-dependent photoresponsivity. The resulting CPL photodetector exhibited high photoresponsivity of 452 A W^{-1}, large g_{res} as high as 0.21, microampere level photocurrent response, and low operating voltage of 0.01 V.
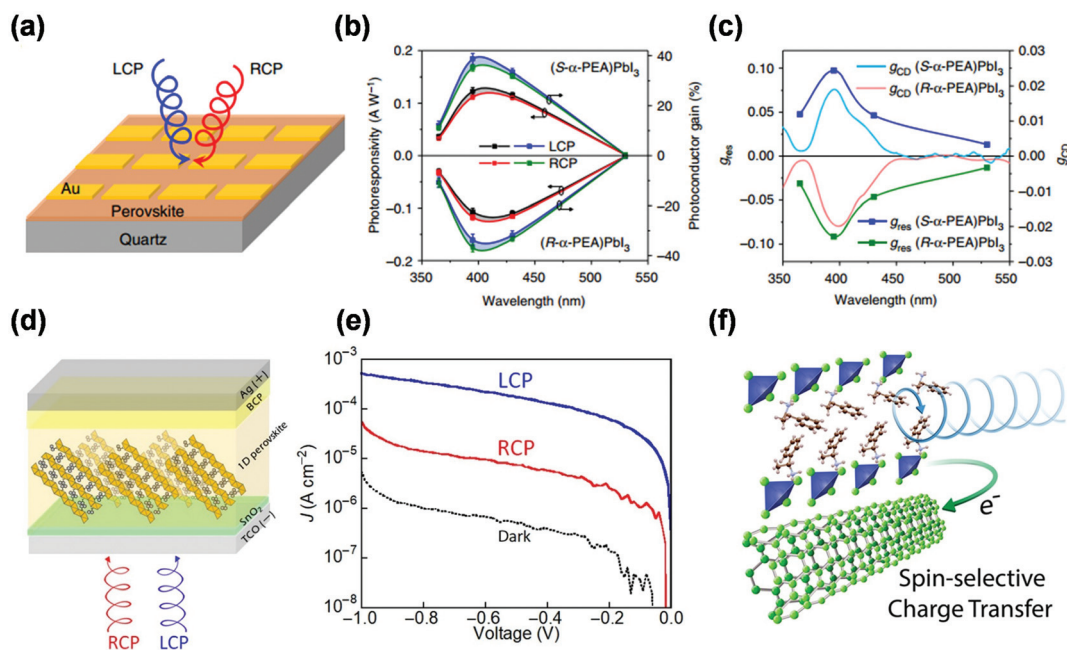

Fig. 10 (a) Schematic of the device structures of photodetectors. (b) The responsivity and photoconductor gain of (R-/S-α-PEA)PbI$_3$-based devices for CPL at different wavelengths, and (c) the dependence of g_{res} on the CPL wavelength. This figure has been adapted/reproduced from ref. 81 with permission from Nature Springer, Copyright 2019. (d) The device structures of photodiodes for the direct CPL detection based on the helical 1D (S-NEA)PbI$_3$ perovskite, and corresponding (e) J–V curves under dark and CPLs (395 nm, 1.0 mW cm^{-2}). This figure has been adapted/reproduced from ref. 78 with permission from Science, Copyright 2020. (f) Schematic illustration of the photoexcited electron transfer at chiral (MBA)$_2$CuCl$_4$/SWCNT heterostructures interface in CPL photodetectors. This figure has been adapted/reproduced from ref. 64 with permission from American Chemical Society, Copyright 2021.

It is worth noting that crystal engineering is shown to be important to increase the CD strength of chiral MHS and thus the performances of CPL photodetectors. Reported strategies include crystalline composition control for the synthesis of lead-free 2D $(R\text{-}\beta\text{-MPA})_4\text{AgBiI}_8$ double perovskites,[59] crystallization dynamics modulation to obtain parallel-oriented chiral quasi-2D $(R\text{-}\beta\text{-MPA})_2\text{MAPb}_2\text{I}_7$ perovskite film,[85] as well as controllable crystal assembly/array of 2D perovskite nanowires arrays for arbitrary light detection.[73] For example, Zhao et al. developed highly sensitive photodetectors for linearly/circularly polarized light detection based on the solution-processed chiral 2D $(R\text{-}\alpha\text{-PEA})_2\text{PbI}_4$ perovskite nanowire arrays.[73] The incorporation of chiral-α-phenylethylammonium cations first transfers its chirality into the inorganic metal–halide layer, guaranteeing the optical activity in inorganic sublattice. Meanwhile, because of single crystallinity and strict crystallographic orientation in nanowires, the resulted CPL photodetectors exhibited a superhigh responsivity of 47.1 A W^{-1} and specific detectivity of 1.24×10^{13} Jones, and the maximum anisotropy factor of responsivity was 0.15 for CPL emission, respectively. Interestingly, the strictly aligned nanowires even show large polarization ratio of 1.6 to linearly polarized light owing to the anisotropic dielectric function.

Fig. 11 CISS effects in photovoltaic devices. (a) Schematic illustration of the structures of spin photovoltaic device. $I\text{–}V$ responses of spin devices for dark and left/right-handed circular polarized lights (20 mW cm^{-2}) based on (b) $(rac\text{-MBA})_2\text{PbI}_4$, (c) $(R\text{-MBA})_2\text{PbI}_4$, and (d) $(S\text{-MBA})_2\text{PbI}_4$, and the insets are corresponding magnified view around 0 V. This figure has been adapted/reproduced from ref. 110 with permission from American Chemical Society, Copyright 2021.

5.2. Spintronic devices

Endowing spin control in chiral MHS-based optoelectronic device can fabricate spin-dependent electronic devices, or spintronic devices. Recently, the CISS effect were demonstrated in various spintronic applications based on chiral MHS.

5.2.1. Spin-photovoltaic devices. Spin-dependent electrical properties in chiral 2D-MHS was demonstrated in a working photovoltaic device.[84,110] Vardeny and co-workers reported the spin-dependent photovoltaic devices based on chiral 2D $(R\text{-}/S\text{-MBA})_2\text{PbI}_4$ (Fig. 11). They observed ca. 10% difference of photocurrent $(\Delta I/I)$ in photovoltaic devices under illumination of right and left-handed CPL, which was attributed to CISS effect.[110] In contrast, the light-helicity-dependent photovoltaic response was not observed in achiral $(rac\text{-MBA})_2\text{PbI}_4$-based photovoltaic device. In addition, photogalvanic measurements indicate a chirality-induced circular photogalvanic effect (CPGE) that originates from the Rashba splitting that occurs in the electronic bands of these compounds.[110]

5.2.2. Spin-valve devices. Traditional spin-valve devices typically require two ferromagnetic electrodes. In 2019, Lu et al. constructed modified spin-valve devices with one ferromagnetic electrode (NiFe) and a chiral 2D hybrid perovskite layer. The opposite magnetoresistance (MR) responses were found in $(R\text{-MBA})_2\text{PbI}_4$ and $(S\text{-MBA})_2\text{PbI}_4$-based devices, which resulted from CISS (Fig. 12).[20] Furthermore, chiral $(MBA)_2\text{PbI}_4$-based device exhibits weak thickness-dependence of MR response, different from traditional spin-valve devices, which stems from two competing processes between spin selectivity through each chiral layer and spin relaxation through each inorganic layer with strong SOC. However, the relative MR% change is relatively small in their spin-valve devices.
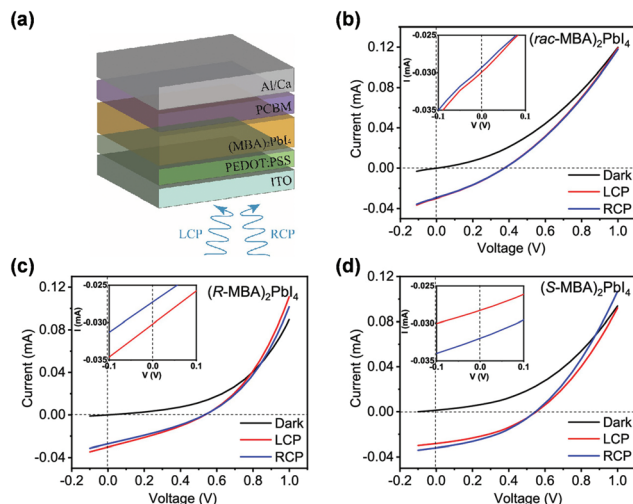
5.2.3. Spin-LED devices. Spin-polarized light-emitting diodes (i.e., spin LED) that emit CPL can be realized when the spin-polarized carrier pairs are injected into the emitting layer in LED devices. Traditional spin-LED requires external magnetic field or ferromagnetic contacts and extreme temperatures to generate spin polarized carriers at the interface. Several previous reports also demonstrated that 3D MHS can be employed in spin-LED devices by applying external magnetic field[111] or coupling traditional LED device with magnetic tunnel junctions.[112] Recently, Kim et al. demonstrated a new concept, where spin-polarized carriers can be generated by chiral MHS through the CISS effect and achieved circularly-polarized electroluminescence in a spin-LED at room temperature (Fig. 13a and b).[113] Their spin-LED consists of a layer of chiral $(R\text{-}/S\text{-MBA})_2\text{PbI}_4$ as the spin-polarization layer and a layer of colloidal CsPbI_3 NCs as the emitting layer, and most importantly, it does not require magnetic field or ferromagnetic contacts. They observe a >80% spin-polarized holes at the interface, where the spin-polarization can be tuned by the handedness of chiral MHS. Spin-polarized holes are then recombined with electrons at the emitting layer, generating a spin polarization degree of circularly-polarized electroluminescence of ±2.6% (Fig. 13c and d) at room temperature, which is comparable to the state-of-the-art spin-LED based on traditional GaAs semiconductors under magnetic fields. The spin-LEDs exhibited a turn-on voltage of only 2.4 V, and external quantum efficiencies of 10.05%, 10.53%, and 11.05% for R-, S-, and $rac\text{-}(MBA)_2\text{PbI}_4$ CISS layer-based LEDs, respectively, which are among the highest EQE values in reported pure CsPbI_3 NCs-based LEDs.
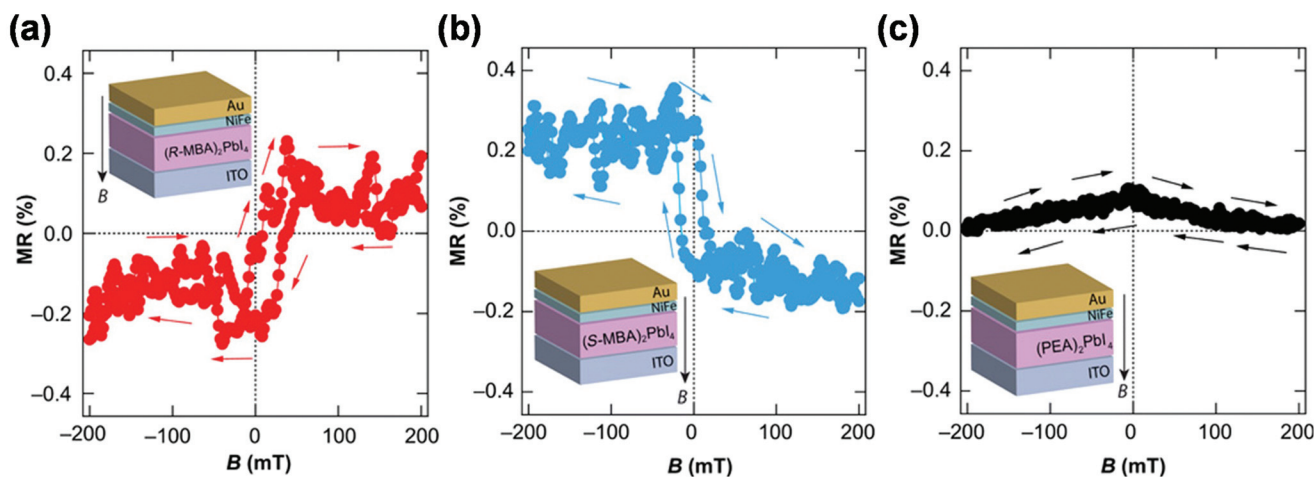
Fig. 12 The MR response towards the magnetic field in spin-valve devices based on the (a) $(R\text{-MBA})_2PbI_4$, (b) $(S\text{-MBA})_2PbI_4$ and (c) achiral $(PEA)_2PbI_4$ perovskites, and the insets are the corresponding device structures. This figure has been adapted/reproduced from ref. 20 with permission from Science, Copyright 2019.
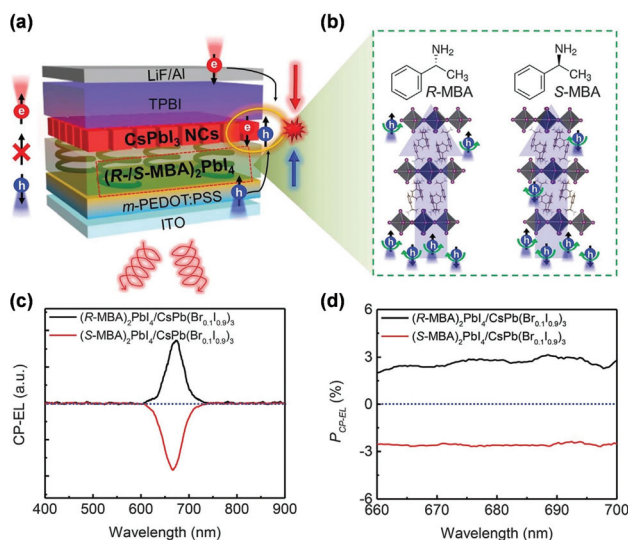

Fig. 13 (a) Schematic illustration of spin-polarized charge injection and CP–EL emission in spin-LED. (b) The structures of chiral R-/S-MBA molecules and 2D $(R\text{-}/S\text{-MBA})_2PbI_4$ perovskites. (c) The CP–EL spectra and (d) EL polarization degree (P_{CP-EL}) of spin-LED based on CISS layer/ $CsPbI_3$ NCs heterostructures. This figure has been adapted/reproduced from ref. 113 with permission from Science, Copyright 2021.

6. Conclusions and perspectives

In this Minireview, we summarized recent advances in using chiral MHS for spin control in various photonic and electronic processes. We discussed strategies that endow chirality in MHS based on different compositions and morphologies. The imprinted chirality in MHS enables spin selectivity in absorption (CD), emission (CPL emission), and electron transport processes mediated by CISS. We presented recent progresses in demonstrating these spin-selective processes in various optoelectronic and spintronic devices. Many progresses have

been achieved in recent years in the development and utilization of these chiral MHS; however, there are still several challenges to be addressed in order to make them truly practical for the next-generation opto-electronic devices where spin control is a critical component.

6.1. Overcome synthetic limitations

We lack synthesis methods for a large library of homochiral hybrid semiconductors. Existing synthesis methods are based on the incorporation of enantiopure starting materials, which could be challenging to obtain. Many chiral MHS are still not accessible by traditional solution methods. For instance, chiral 2D metal–halide perovskites with inorganic layer thickness larger than 2 (i.e., $n > 2$) are still not isolated in pure phase, let alone the "hypothetical" chiral 3D MHS. These synthetic difficulties have largely limited the materials discovery of chiral MHS. Synthesis of these challenging chiral MHS might be the key to address their poor conductivity and photo-luminescence quantum yields, which will excel their applications beyond current optoelectronic devices.

6.2. Understand the chirality origin and structure–chiroptical–activity relationships

The precise relationship between structure chirality, composition, dimensionality, and chiroptical activity remains unclear. Although many chiral MHS are reported in literature, there is no unambiguous understanding of the chirality origin or the chirality transfer mechanism in this family of materials. The design rules of obtaining chiral MHS with higher dissymmetry factor beyond current limits remains unresolved. Along these lines, the work of Mitzi and co-workers[114,115] and Chiu[71] should have interesting implications on uncovering the origin of chirality in these materials. Theoretical efforts should also be integrated to unveil the structure–chirality relationships.

6.3. Understand the chirality–spin-selectivity relationship

There lacks quantitative understanding of the relationship between chirality and spin-selectivity in these optical and electrical-transport processes. The precise model of CISS remains unclear in these chiral MHS, which requires more efforts to quantitatively measure and model the CISS effect both experimentally and theoretically. Previous reports have shown a positive correlation between chiroptical activity and spin selectivity in chiral small molecules and NCs,[116] but the relationship remains unknown in these chiral MHS systems. These experimental investigations should be corroborated with recent theoretical efforts that model CISS based on geometrical helicity,[30,117] spin–orbital couplings,[118,119] electron–phonon couplings,[120,121] and electric field models.[122] The combined effort from experiment and theory would help to unveil the mystery of the CISS effect.

6.4. Explore spin-selective process beyond current optoelectronic devices

In addition to spin-dependent optoelectronic devices, the CISS effect of chiral MHS should also be explored in other spin-sensitive processes, such as chemical transformations, spin-enhanced electrochemistry, and enantiospecific separation, which have been demonstrated with chiral small molecules.

Author contributions

T. F. and H. L. decided the theme and content of the review, and wrote the manuscript. Z. W. prepared a part of figures. Z. Z. and J. X. revised the review.

Conflicts of interest

There are no conflicts to declare.

Acknowledgements

References

1 Y. Fu, H. Zhu, J. Chen, M. P. Hautzinger, X. Y. Zhu and S. Jin, *Nat. Rev. Mater.*, 2019, **4**, 169–188.

2 Y. Zhao and K. Zhu, *Chem. Soc. Rev.*, 2016, **45**, 655–689.

3 Q. Zeng, X. Zhang, X. Feng, S. Lu, Z. Chen, X. Yong, S. A. T. Redfern, H. Wei, H. Wang, H. Shen, W. Zhang, W. Zheng, H. Zhang, J. S. Tse and B. Yang, *Adv. Mater.*, 2018, **30**, 1705393.

4 A. Kojima, K. Teshima, Y. Shirai and T. Miyasaka, *J. Am. Chem. Soc.*, 2009, **131**, 6050–6051.

5 M. M. Lee, J. Teuscher, T. Miyasaka, T. N. Murakami and H. J. Snaith, *Science*, 2012, **338**, 643–647.

6 H. S. Kim, C. R. Lee, J. H. Im, K. B. Lee, T. Moehl, A. Marchioro, S. J. Moon, R. Humphry-Baker, J. H. Yum, J. E. Moser, M. Gratzel and N. G. Park, *Sci. Rep.*, 2012, **2**, 591.

7 K. Liao, X. Hu, Y. Cheng, Z. Yu, Y. Xue, Y. Chen and Q. Gong, *Adv. Opt. Mater.*, 2019, **7**, 1900350.

8 J. Ma, H. Wang and D. Li, *Adv. Mater.*, 2021, **33**, e2008785.

9 S. Ma, J. Ahn and J. Moon, *Adv. Mater.*, 2021, e2005760.

10 Y. Dong, Y. Zhang, X. Li, Y. Feng, H. Zhang and J. Xu, *Small*, 2019, **15**, e1902237.

11 Y. Dang, X. Liu, B. Cao and X. Tao, *Matter*, 2021, **4**, 794–820.

12 G. Long, R. Sabatini, M. I. Saidaminov, G. Lakhwani, A. Rasmita, X. Liu, E. H. Sargent and W. Gao, *Nat. Rev. Mater.*, 2020, **5**, 423–439.

13 D. Qi, A. Kenaan, D. Cui and J. Song, *Nano Energy*, 2018, **52**, 142–152.

14 K. Michaeli, N. Kantor-Uriel, R. Naaman and D. H. Waldeck, *Chem. Soc. Rev.*, 2016, **45**, 6478–6487.

15 C. Hao, L. Xu, H. Kuang and C. Xu, *Adv. Mater.*, 2020, **32**, e1802075.

16 W. Ma, L. Xu, A. F. de Moura, X. Wu, H. Kuang, C. Xu and N. A. Kotov, *Chem. Rev.*, 2017, **117**, 8041–8093.

17 J. Liu, L. Yang, P. Qin, S. Zhang, K. K. L. Yung and Z. Huang, *Adv. Mater.*, 2021, e2005506.

18 J. Ahn, E. Lee, J. Tan, W. Yang, B. Kim and J. Moon, *Mater. Horiz.*, 2017, **4**, 851–856.

19 G. Long, C. Jiang, R. Sabatini, Z. Yang, M. Wei, L. N. Quan, Q. Liang, A. Rasmita, M. Askerka, G. Walters, X. Gong, J. Xing, X. Wen, R. Quintero-Bermudez, H. Yuan, G. Xing, X. R. Wang, D. Song, O. Voznyy, M. Zhang, S. Hoogland, W. Gao, Q. Xiong and E. H. Sargent, *Nat. Photonics*, 2018, **12**, 528–533.

20 H. Lu, J. Wang, C. Xiao, X. Pan, X. Chen, R. Brunecky, J. J. Berry, K. Zhu, M. C. Beard and Z. V. Vardeny, *Sci. Adv.*, 2019, **5**, eaay0571.

21 K. Y. Bliokh, F. J. Rodríguez-Fortuño, F. Nori and A. V. Zayats, *Nat. Photonics*, 2015, **9**, 796–808.

22 P. Odenthal, W. Talmadge, N. Gundlach, R. Wang, C. Zhang, D. Sun, Z.-G. Yu, Z. Valy Vardeny and Y. S. Li, *Nat. Phys.*, 2017, **13**, 894–899.

23 Y. Zhai, S. Baniya, C. Zhang, J. Li, P. Haney, C.-X. Sheng, E. Ehrenfreund and Z. V. Vardeny, *Sci. Adv.*, 2017, **3**, e1700704.

24 D. Niesner, M. Wilhelm, I. Levchuk, A. Osvet, S. Shrestha, M. Batentschuk, C. Brabec and T. Fauster, *Phys. Rev. Lett.*, 2016, **117**, 126401.

25 X. Liu, A. Chanana, U. Huynh, F. Xue, P. Haney, S. Blair, X. Jiang and Z. V. Vardeny, *Nat. Commun.*, 2020, **11**, 323.

26 F. Zheng, L. Z. Tan, S. Liu and A. M. Rappe, *Nano Lett.*, 2015, **15**, 7794–7800.

27 D. Niesner, M. Hauck, S. Shrestha, I. Levchuk, G. J. Matt, A. Osvet, M. Batentschuk, C. Brabec, H. B. Weber and T. Fauster, *Proc. Natl. Acad. Sci. U. S. A.*, 2018, **115**, 9509–9514.

28 H. Lu, C. Xiao, R. Song, T. Li, A. E. Maughan, A. Levin, R. Brunecky, J. J. Berry, D. B. Mitzi, V. Blum and M. C. Beard, *J. Am. Chem. Soc.*, 2020, **142**, 13030–13040.

29 Y. Lu, Q. Wang, R. Chen, L. Qiao, F. Zhou, X. Yang, D. Wang, H. Cao, W. He, F. Pan, Z. Yang and C. Song, *Adv. Funct. Mater.*, 2021, 2104605.

30 Z. G. Yu, *J. Phys. Chem. Lett.*, 2020, **11**, 8638–8646.

31 R. Naaman, Y. Paltiel and D. H. Waldeck, *Acc. Chem. Res.*, 2020, **53**, 2659–2667.

32 S. Dalum and P. Hedegard, *Nano Lett.*, 2019, **19**, 5253–5259.

33 C. Fontanesi, E. Capua, Y. Paltiel, D. H. Waldeck and R. Naaman, *Adv. Mater.*, 2018, **30**, e1707390.

34 R. Naaman, Y. Paltiel and D. H. Waldeck, *Nat. Rev. Chem.*, 2019, **3**, 250–260.

35 R. A. Rosenberg, D. Mishra and R. Naaman, *Angew. Chem., Int. Ed.*, 2015, **54**, 7295–7298.

36 R. Naaman and D. H. Waldeck, *Annu. Rev. Phys. Chem.*, 2015, **66**, 263–281.

37 B. Göhler, V. Hamelbeck, T. Z. Markus, M. Kettner, G. F. Hanne, Z. Vager, R. Naaman and H. Zacharias, *Science*, 2011, **331**, 894–897.

38 K. Banerjee-Ghosh, O. B. Dor, F. Tassinari, E. Capua, S. Yochelis, A. Capua, S.-H. Yang, S. S. P. Parkin, S. Sarkar, L. Kronik, L. T. Baczewski, R. Naaman and Y. Paltiel, *Science*, 2018, **360**, 1331–1334.

39 R. Naaman and D. H. Waldeck, *J. Phys. Chem. Lett.*, 2012, **3**, 2178–2187.

40 R. Naaman, Y. Paltiel and D. H. Waldeck, *J. Phys. Chem. Lett.*, 2020, **11**, 3660–3666.

41 J. M. Abendroth, D. M. Stemer, B. P. Bloom, P. Roy, R. Naaman, D. H. Waldeck, P. S. Weiss and P. C. Mondal, *ACS Nano*, 2019, **13**, 4928–4946.

42 P. C. Mondal, C. Fontanesi, D. H. Waldeck and R. Naaman, *Acc. Chem. Res.*, 2016, **49**, 2560–2568.

43 K. Ray, S. P. Ananthavel, D. H. Waldeck and R. Naaman, *Science*, 1999, **283**, 814–816.

44 H. Einati, D. Mishra, N. Friedman, M. Sheves and R. Naaman, *Nano Lett.*, 2015, **15**, 1052–1056.

45 M. Eckshtain-Levi, E. Capua, S. Refaely-Abramson, S. Sarkar, Y. Gavrilov, S. P. Mathew, Y. Paltiel, Y. Levy, L. Kronik and R. Naaman, *Nat. Commun.*, 2016, **7**, 10744.

46 D. Mishra, T. Z. Markus, R. Naaman, M. Kettner, B. Göhler, H. Zacharias, N. Friedman, M. Sheves and C. Fontanesi, *Proc. Natl. Acad. Sci. U. S. A.*, 2013, **110**, 14872–14876.

47 B. P. Bloom, V. Kiran, V. Varade, R. Naaman and D. H. Waldeck, *Nano Lett.*, 2016, **16**, 4583–4589.

48 D. Fu, J. Xin, Y. He, S. Wu, X. Zhang, X. M. Zhang and J. Luo, *Angew. Chem., Int. Ed.*, 2021, **60**, 20021–20026.

49 C. Yuan, X. Li, S. Semin, Y. Feng, T. Rasing and J. Xu, *Nano Lett.*, 2018, **18**, 5411–5417.

50 N. Dehnhardt, M. Axt, J. Zimmermann, M. Yang, G. Mette and J. Heine, *Chem. Mater.*, 2020, **32**, 4801–4807.

51 Y. L. Zeng, X. Q. Huang, C. R. Huang, H. Zhang, F. Wang and Z. X. Wang, *Angew. Chem., Int. Ed.*, 2021, **60**, 10730–10735.

52 Y. Y. Tang, Y. Ai, W. Q. Liao, P. F. Li, Z. X. Wang and R. G. Xiong, *Adv. Mater.*, 2019, **31**, e1902163.

53 J. X. Gao, W. Y. Zhang, Z. G. Wu, Y. X. Zheng and D. W. Fu, *J. Am. Chem. Soc.*, 2020, **142**, 4756–4761.

54 Y. Hu, F. Florio, Z. Chen, W. A. Phelan, M. A. Siegler, Z. Zhou, Y. Guo, R. Hawks, J. Jiang, J. Feng, L. Zhang, B. Wang, Y. Wang, D. Gall, E. F. Palermo, Z. Lu, X. Sun, T.-M. Lu, H. Zhou, Y. Ren, E. Wertz, R. Sundararaman and J. Shi, *Sci. Adv.*, 2020, **6**, eaay4213.

55 S. Chen and G. Shi, *Adv. Mater.*, 2017, **29**, e1605448.

56 Z. Shi, J. Guo, Y. Chen, Q. Li, Y. Pan, H. Zhang, Y. Xia and W. Huang, *Adv. Mater.*, 2017, **29**, 1605005.

57 Z. Chu, X. Chu, Y. Zhao, Q. Ye, J. Jiang, X. Zhang and J. You, *Small Struct.*, 2021, **2**, 2000133.

58 H. Lin, C. Zhou, Y. Tian, T. Siegrist and B. Ma, *ACS Energy Lett.*, 2017, **3**, 54–62.

59 D. Li, X. Liu, W. Wu, Y. Peng, S. Zhao, L. Li, M. Hong and J. Luo, *Angew. Chem., Int. Ed.*, 2021, **60**, 8415–8418.

60 T. H. Moon, S. J. Oh and K. M. Ok, *ACS Omega*, 2018, **3**, 17895–17903.

61 L. Yao, Z. Zeng, C. Cai, P. Xu, H. Gu, L. Gao, J. Han, X. Zhang, X. Wang, X. Wang, A. Pan, J. Wang, W. Liang, S. Liu, C. Chen and J. Tang, *J. Am. Chem. Soc.*, 2021, **143**, 16095–16104.

62 K. Taniguchi, M. Nishio, N. Abe, P. J. Huang, S. Kimura, T. H. Arima and H. Miyasaka, *Angew. Chem., Int. Ed.*, 2021, **60**, 14350–14354.

63 F. Hajlaoui, I. B. Hadj Sadok, H. A. Aeshah, N. Audebrand, T. Roisnel and N. Zouari, *J. Mol. Struct.*, 2019, **1182**, 47–53.

64 J. Hao, H. Lu, L. Mao, X. Chen, M. C. Beard and J. L. Blackburn, *ACS Nano*, 2021, **15**, 7608–7617.

65 L. Yao, G. Niu, J. Li, L. Gao, X. Luo, B. Xia, Y. Liu, P. Du, D. Li, C. Chen, Y. Zheng, Z. Xiao and J. Tang, *J. Phys. Chem. Lett.*, 2020, **11**, 1255–1260.

66 M. Takahashi, N. Hoshino, K. Sambe, T. Takeda and T. Akutagawa, *Inorg. Chem.*, 2020, **59**, 11606–11615.

67 L. S. Li, Y. H. Tan, W. J. Wei, H. Q. Gao, Y. Z. Tang and X. B. Han, *ACS Appl. Mater. Interfaces*, 2021, **13**, 2044–2051.

68 H. Peng, H. Cheng, Y.-H. Liu, M.-J. Yang, W.-Q. Liao and Y. Ai, *J. Mater. Chem. C*, 2021, **9**, 1918–1922.

69 J. Ahn, S. Ma, J. Y. Kim, J. Kyhm, W. Yang, J. A. Lim, N. A. Kotov and J. Moon, *J. Am. Chem. Soc.*, 2020, **142**, 4206–4212.

70 J. Ma, C. Fang, C. Chen, L. Jin, J. Wang, S. Wang, J. Tang and D. Li, *ACS Nano*, 2019, **13**, 3659–3665.

71 J. T. Lin, D. G. Chen, L. S. Yang, T. C. Lin, Y. H. Liu, Y. C. Chao, P. T. Chou and C. W. Chiu, *Angew. Chem., Int. Ed.*, 2021, **60**, 21434–21440.

72 J. Wang, C. Fang, J. Ma, S. Wang, L. Jin, W. Li and D. Li, *ACS Nano*, 2019, **13**, 9473–9481.

73 Y. Zhao, Y. Qiu, J. Feng, J. Zhao, G. Chen, H. Gao, Y. Zhao, L. Jiang and Y. Wu, *J. Am. Chem. Soc.*, 2021, **143**, 8437–8445.

74 Y. Peng, X. Liu, L. Li, Y. Yao, H. Ye, X. Shang, X. Chen and J. Luo, *J. Am. Chem. Soc.*, 2021, **143**, 14077–14082.

75 Y. Liu, C. Wang, Y. Guo, L. Ma, C. Zhou, Y. Liu, L. Zhu, X. Li, M. Zhang and G. Zhao, *J. Mater. Chem. C*, 2020, **8**, 5673–5680.

76 F. F. Gao, X. Li, Y. Qin, Z. G. Li, T. M. Guo, Z. Z. Zhang, G. D. Su, C. Jiang, M. Azeem, W. Li, X. Wu and X. H. Bu, *Adv. Opt. Mater.*, 2021, 2100003.

77 Y. Dang, X. Liu, Y. Sun, J. Song, W. Hu and X. Tao, *J. Phys. Chem. Lett.*, 2020, **11**, 1689–1696.

78 A. Ishii and T. Miyasaka, *Sci. Adv.*, 2020, **6**, eabd3274.

79 A. Lemmerer and D. G. Billing, *J. Chem.*, 2013, **66**, 262–272.

80 D. G. Billing and A. Lemmerer, *CrystEngComm*, 2006, **8**, 686–695.

81 C. Chen, L. Gao, W. Gao, C. Ge, X. Du, Z. Li, Y. Yang, G. Niu and J. Tang, *Nat. Commun.*, 2019, **10**, 1927.

82 H. Peng, Y.-H. Liu, X.-Q. Huang, Q. Liu, Z.-H. Yu, Z.-X. Wang and W.-Q. Liao, *Mater. Chem. Front.*, 2021, **5**, 4756–4763.

83 Y. Peng, Y. Yao, L. Li, Z. Wu, S. Wang and J. Luo, *J. Mater. Chem. C*, 2018, **6**, 6033–6037.

84 P. J. Huang, K. Taniguchi and H. Miyasaka, *J. Am. Chem. Soc.*, 2019, **141**, 14520–14523.

85 L. Wang, Y. Xue, M. Cui, Y. Huang, H. Xu, C. Qin, J. Yang, H. Dai and M. Yuan, *Angew. Chem., Int. Ed.*, 2020, **59**, 6442–6450.

86 D. Di Nuzzo, L. Cui, J. L. Greenfield, B. Zhao, R. H. Friend and S. C. J. Meskers, *ACS Nano*, 2020, **14**, 7610–7616.

87 H. Ohsumi, A. Tokuda, S. Takeshita, M. Takata, M. Suzuki, N. Kawamura, Y. Kousaka, J. Akimitsu and T. H. Arima, *Angew. Chem., Int. Ed.*, 2013, **52**, 8718–8721.

88 H.-R. Zhao, D.-P. Li, X.-M. Ren, Y. Song and W.-Q. Jin, *J. Am. Chem. Soc.*, 2010, **132**, 18–19.

89 N. Mercier, A. L. Barres, M. Giffard, I. Rau, F. Kajzar and B. Sahraoui, *Angew. Chem., Int. Ed.*, 2006, **45**, 2100–2103.

90 Y. H. Kim, Y. Zhai, E. A. Gaulding, S. N. Habisreutinger, T. Moot, B. A. Rosales, H. Lu, A. Hazarika, R. Brunecky, L. M. Wheeler, J. J. Berry, M. C. Beard and J. M. Luther, *ACS Nano*, 2020, **14**, 8816–8825.

91 T. He, J. Li, X. Li, C. Ren, Y. Luo, F. Zhao, R. Chen, X. Lin and J. Zhang, *Appl. Phys. Lett.*, 2017, **111**, 151102.

92 W. Chen, S. Zhang, M. Zhou, T. Zhao, X. Qin, X. Liu, M. Liu and P. Duan, *J. Phys. Chem. Lett.*, 2019, **10**, 3290–3295.

93 Y. Shi, P. Duan, S. Huo, Y. Li and M. Liu, *Adv. Mater.*, 2018, **30**, e1705011.

94 C. T. Wang, K. Chen, P. Xu, F. Yeung, H. S. Kwok and G. Li, *Adv. Funct. Mater.*, 2019, **29**, 1903155.

95 X. Yang, M. Zhou, Y. Wang and P. Duan, *Adv. Mater.*, 2020, **32**, e2000820.

96 B. Zhao, X. Gao, K. Pan and J. Deng, *ACS Nano*, 2021, **15**, 7463–7471.

97 P. Liu, W. Chen, Y. Okazaki, Y. Battie, L. Brocard, M. Decossas, E. Pouget, P. Muller-Buschbaum, B. Kauffmann, S. Pathan, T. Sagawa and R. Oda, *Nano Lett.*, 2020, **20**, 8453–8460.

98 D. H. Waldeck, R. Naaman and Y. Paltiel, *APL Mater.*, 2021, **9**, 040902.

99 A. Kumara, E. Capuaa, M. K. Kesharwanib, J. M. L. Martinb, E. Sitbonc, D. H. Waldeckd and R. Naamana, *Proc. Natl. Acad. Sci. U. S. A.*, 2017, **114**, 2474–2478.

100 J. Fransson, *Nano Lett.*, 2021, **21**, 3026–3032.

101 P. C. Mondal, P. Roy, D. Kim, E. E. Fullerton, H. Cohen and R. Naaman, *Nano Lett.*, 2016, **16**, 2806–2811.

102 S. Mishra, S. Pirbadian, A. K. Mondal, M. Y. El-Naggar and R. Naaman, *J. Am. Chem. Soc.*, 2019, **141**, 19198–19202.

103 P. C. Mondal, N. Kantor-Uriel, S. P. Mathew, F. Tassinari, C. Fontanesi and R. Naaman, *Adv. Mater.*, 2015, **27**, 1924–1927.

104 A. K. Mondal, N. Brown, S. Mishra, P. Makam, D. Wing, S. Gilead, Y. Wiesenfeld, G. Leitus, L. J. W. Shimon, R. Carmieli, D. Ehre, G. Kamieniarz, J. Fransson, O. Hod, L. Kronik, E. Gazit and R. Naaman, *ACS Nano*, 2020, **14**, 16624–16633.

105 T. S. Metzger, S. Mishra, B. P. Bloom, N. Goren, A. Neubauer, G. Shmul, J. Wei, S. Yochelis, F. Tassinari, C. Fontanesi, D. H. Waldeck, Y. Paltiel and R. Naaman, *Angew. Chem., Int. Ed.*, 2020, **59**, 1653–1658.

106 F. Tassinari, D. R. Jayarathna, N. Kantor-Uriel, K. L. Davis, V. Varade, C. Achim and R. Naaman, *Adv. Mater.*, 2018, **30**, e1706423.

107 P. C. Mondal, C. Fontanesi, D. H. Waldeck and R. Naaman, *ACS Nano*, 2015, **9**, 3377–3384.

108 T. P. Fay, *J. Phys. Chem. Lett.*, 2021, **12**, 1407–1412.

109 Z. Huang, B. P. Bloom, X. Ni, Z. N. Georgieva, M. Marciesky, E. Vetter, F. Liu, D. H. Waldeck and D. Sun, *ACS Nano*, 2020, **14**, 10370–10375.

110 J. Wang, H. Lu, X. Pan, J. Xu, H. Liu, X. Liu, D. R. Khanal, M. F. Toney, M. C. Beard and Z. V. Vardeny, *ACS Nano*, 2021, **15**, 588–595.

111 J. Wang, C. Zhang, H. Liu, R. McLaughlin, Y. Zhai, S. R. Vardeny, X. Liu, S. McGill, D. Semenov, H. Guo, R. Tsuchikawa, V. V. Deshpande, D. Sun and Z. V. Vardeny, *Nat. Commun.*, 2019, **10**, 129.

112 C. Zhang, D. Sun and Z. V. Vardeny, *Adv. Electron. Mater.*, 2017, **3**, 1600426.

113 Y.-H. Kim, Y. Zhai, H. Lu, X. Pan, C. Xiao, E. A. Gaulding, S. P. Harvey, J. J. Berry, Z. V. Vardeny, J. M. Luther and M. C. Beard, *Science*, 2021, **371**, 1129–1133.

114 M. K. Jana, R. Song, H. Liu, D. R. Khanal, S. M. Janke, R. Zhao, C. Liu, Z. Valy Vardeny, V. Blum and D. B. Mitzi, *Nat. Commun.*, 2020, **11**, 4699.

115 M. K. Jana, R. Song, Y. Xie, R. Zhao, P. C. Sercel, V. Blum and D. B. Mitzi, *Nat. Commun.*, 2021, **12**, 4982.

116 B. P. Bloom, B. M. Graff, S. Ghosh, D. N. Beratan and D. H. Waldeck, *J. Am. Chem. Soc.*, 2017, **139**, 9038–9043.

117 R. Gutierrez, E. Díaz, R. Naaman and G. Cuniberti, *Phys. Rev. B: Condens. Matter Mater. Phys.*, 2012, **85**, 081404(R).

118 S. Alwan and Y. Dubi, *J. Am. Chem. Soc.*, 2021, **143**, 14235–14241.

119 M. S. Zollner, A. Saghatchi, V. Mujica and C. Herrmann, *J. Chem. Theory Comput.*, 2020, **16**, 7357–7371.

120 J. Fransson, *J. Phys. Chem. Lett.*, 2019, **10**, 7126–7132.

121 J. Fransson, *Phys. Rev. B*, 2020, **102**, 235416.

122 K. Michaeli, D. N. Beratan, D. H. Waldeck and R. Naaman, *Proc. Natl. Acad. Sci. U. S. A.*, 2019, **116**, 5931–5936.